Journal of Power Sources 191 (2009) 42–50

Contents lists available at ScienceDirect

Journal of Power Sources

journal homepage: www.elsevier.com/locate/jpowsour

Simulation of the current distribution in lead-acid batteries to investigate the dynamic charge acceptance in flooded SLI batteries

Julia Kowal[a,*], Dominik Schulte[a], Dirk Uwe Sauer[a], Eckhard Karden[b]

[a] Electrochemical Energy Conversion and Storage Systems Group, Institute for Power Electronics and Electrical Drives (ISEA), RWTH Aachen University, 52066 Aachen, Germany
[b] Ford Research and Advanced Engineering Europe, Aachen, Germany

ARTICLE INFO

Article history:
Received 29 September 2008
Received in revised form
21 November 2008
Accepted 4 December 2008
Available online 9 December 2008

Keywords:
Lead-acid battery
Dynamic charge acceptance
Acid stratification
Current distribution
Spatially resolved model

ABSTRACT

Measurements show that the dynamic charge acceptance (DCA) of flooded SLI lead-acid batteries during micro-cycling in conventional and micro-hybrid vehicles is strongly dependent on the short-term history, such as previous charge or discharge, current rate, lowest state of charge in the last 24 h and more. Factors of 10 have been reported. Inhomogeneous current distribution, especially as a result of acid stratification, has been suggested to explain the DCA variability.

This hypothesis was investigated by simulation of a two-dimensional macrohomogeneous model. It provides a spatial resolution of three elements in horizontal direction in each electrode and three elements in vertical direction. For an existing set of parameters, different current profiles were analyzed with regard to the current distribution during charging and discharging.

In these simulations, a strong impact of the short-term history on current, charge and acid density distribution was found as well as a strong influence of micro-cycles on both charge distribution and acid stratification.

1. Introduction

In micro-hybrid[1] automotive applications, lead-acid batteries are typically used in partial state of charge (PSOC) operation. This implies micro-cycling and very few full charges. As a consequence, batteries suffer from sulphation of the lower part of the electrodes as a main ageing mechanism [1,2]. Another effect of PSOC operation is a strongly varying dynamic charge acceptance (DCA) depending on the short-term history, which is the focus of this paper. We define DCA as the amount of charge that is actually charged to the battery during regenerative braking phases of a driving cycle, e.g. NEDC, divided by the amount of charge that could be provided by the generator. Factors of five between different short-term history conditions have been shown by Sauer [3] and unpublished results of the authors exhibit even a factor of 10. Short-term history in this context means e.g. if the battery was charged or discharged before the regenerative braking phase, if it was deeply discharged within the last days, which charge and discharge current rate were applied and so on. "Short-term" means a time span of up to 2 or 3 days, maybe even a week.

In a previous paper [4], some investigations of the effect of short-term history on DCA have been reported. Inhomogeneous current distribution as a result of acid stratification and the assumption that freshly discharged active material has a higher charge acceptance than active material that was discharged a longer time ago have been suggested as an explanation for this behaviour. If charging takes place in another location than the previous discharge, the freshly discharged material is not available for charging and consequently the charge acceptance is low. In this paper, this hypothesis is investigated in simulations with a spatially resolved physicochemical model, where high rate micro-cycles were simulated after different preconditions to analyse the influence of various parameters such as current rate, SOC preconditioning and initial acid stratification. We only consider conventional flooded batteries without carbon additives. Recently, many authors have reported that carbon additives are beneficial for the charge acceptance of lead-acid batteries [5–8], but as the mechanism is explained in many different ways and not completely understood yet, it is hard to include it in a model.

Many simulation models of lead-acid batteries have been developed and described in the literature. In this paper, we concentrate on the macrohomogeneous modelling approach for porous electrodes developed by Newman and Tiedemann [9] to describe the discharge behaviour of lead-acid batteries. In this approach, which is also called mesoscopic, the porous volume element is interpreted as a superposition of two continua that penetrate each other. One continuum is the electrolyte and the other is the elec-

* Corresponding author. Tel.: +49 241 8096935; fax: +49 241 8092203.
E-mail address: batteries@isea.rwth-aachen.de (J. Kowal).

[1] Microhybrid means the minimum stage of hybridisation with stop start function and minimum regenerative braking.

0378-7753/$ – see front matter © 2008 Elsevier B.V. All rights reserved.
doi:10.1016/j.jpowsour.2008.12.016

trode matrix. All physical variables are described by a spatially continuous function, so that reactions at the phase boundary can be described as a homogeneous reaction in the electrode volume. Newman and Tiedemann only simulated large discharge currents, Sunu [10] extended the approach for small discharge currents and Gu et al. [11] extended the modelling approach for rest and charge. Bernardi et al. [12] proposed a two-dimensional model. Alavyoon et al. [13] investigated free convection and stratification of electrolyte with measurement and simulation. Gu et al. [14] further improved the modelling approach including all aspects of the previous approaches. In all these models, acid movement due to gassing is neglected. Sauer [15–17] proposed a new approach including all relevant mechanisms of acid movement: diffusion, buoyancy, gravity, gassing and ion production and consumption, but with simplified and decoupled equations to reduce the calculation time. Decoupling was realised mainly by neglecting time dependencies within one time step of slowly changing variables. The model of Sauer is used here to investigate local charge, acid density and current distribution during micro-cycling.

Models to simulate the current distribution in lead-acid batteries have also been proposed by several authors: Ball et al. [18] simulated the current density in a positive grid with finite elements method. Král et al. [19] simulated the current distribution in a flat electrode and Křivák et al. [20] simulated the current distribution in a cylindrical cell, both using an equivalent circuit. Boovaragavan and Subramanian [21] simulated the current distribution over a planar electrode in order to find an optimum current profile for maximum mass utilization.

2. Simulation model

The simulation model is based on a resistance network, which is solved in each time step (see Section 2.1). All voltage sources and resistors are calculated in each time step according to the present conditions such as temperature, current, acid concentration, or ageing. Electrolyte concentration is calculated on the basis of the physical laws on diffusion, generation and use of sulphate ions during charging and discharging, gravity and electrolyte mixing by gassing (see Section 2.2). The resolution of the electrical model is fixed to three vertical layers and three horizontal layers in each electrode (Fig. 1, lower picture) while the acid model works with a much finer resolution (Fig. 1, upper picture). In fact, the model is a two-dimensional model and the geometry of the cell is reduced to one single pair of positive and negative plates facing each other. It is assumed that all other pairs of electrodes have similar conditions due to symmetry reasons. Furthermore, as in most previous publications [9–12,14], it is assumed that the current distribution is homogeneous along the width of the electrodes.[2]

Fig. 1 also gives the dimensions of the simulated battery. As can be seen, the size of the visualization of the elements is not representative for the real dimensions. Variations of the battery design influence the simulation results [17], but the general conclusions are valid independently from the design.

The limited resolution of the model is chosen as a compromise between computing speed and accuracy of the model. A detailed

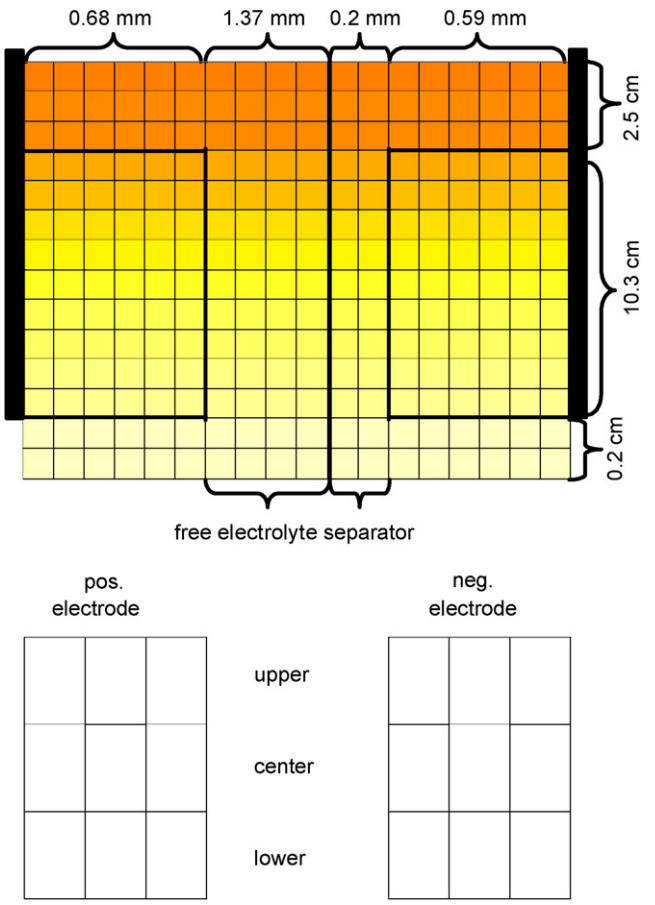

Fig. 1. Spatial resolution for acid density (top) and for current and SOC distribution (bottom). The black lines in the acid density grid indicate the location of the electrodes. Real dimensions for a flooded 12◦V 60 Ah battery are given. This battery is simulated.

temperature model is included as well. This model cannot reflect the dynamic charge acceptance completely due to a missing hardening crystal approach[3] [24], but current distribution and acid density within the cell are represented correctly.The most important parts of the simulation model are described here in detail. Also ageing processes such as corrosion and sulphation are represented in this model, but as they only take place very slowly and only have very little influence during the simulations presented here, they are not illustrated here apart from resistances in Fig. 2.

It is possible to simulate flooded, gel and AGM batteries with this model. Significant differences are mentioned in the description for completeness, but simulations presented in this paper are only performed on the flooded battery with dimensions given in Fig. 1.

2.1. Equivalent electric circuit diagram

Each process in the battery cell and each pathway for electrons or ions are represented by a resistor. Additionally, the sources for the electrochemical equilibrium voltage are included in the equivalent circuit diagram. The complete network is shown in Fig. 2, the meaning and dependencies of the circuit elements are given in Table 1. All voltage sources and resistors are recalculated in each time step based on the local conditions of current flow, potential, acid concen-

[2] This is true only in first order approximation. In reality there are inhomogeneities along the electrode due to asymmetric grids and the position of the current collector, which was demonstrated by several authors [19,22,23]. Also recent unpublished measurements by the authors show inhomogeneous current distribution along the electrodes. However, the general conclusions that can be obtained from the simulation without current distribution along the electrodes are valid as well for real battery operation.

[3] The hardening crystals approach represents the effect that lead-acid batteries show a better charge acceptance after a previous discharge than after a previous pause. It is assumed that sulphate crystals unite with time, thus growing to less and larger crystals, which are harder to dissolve again.

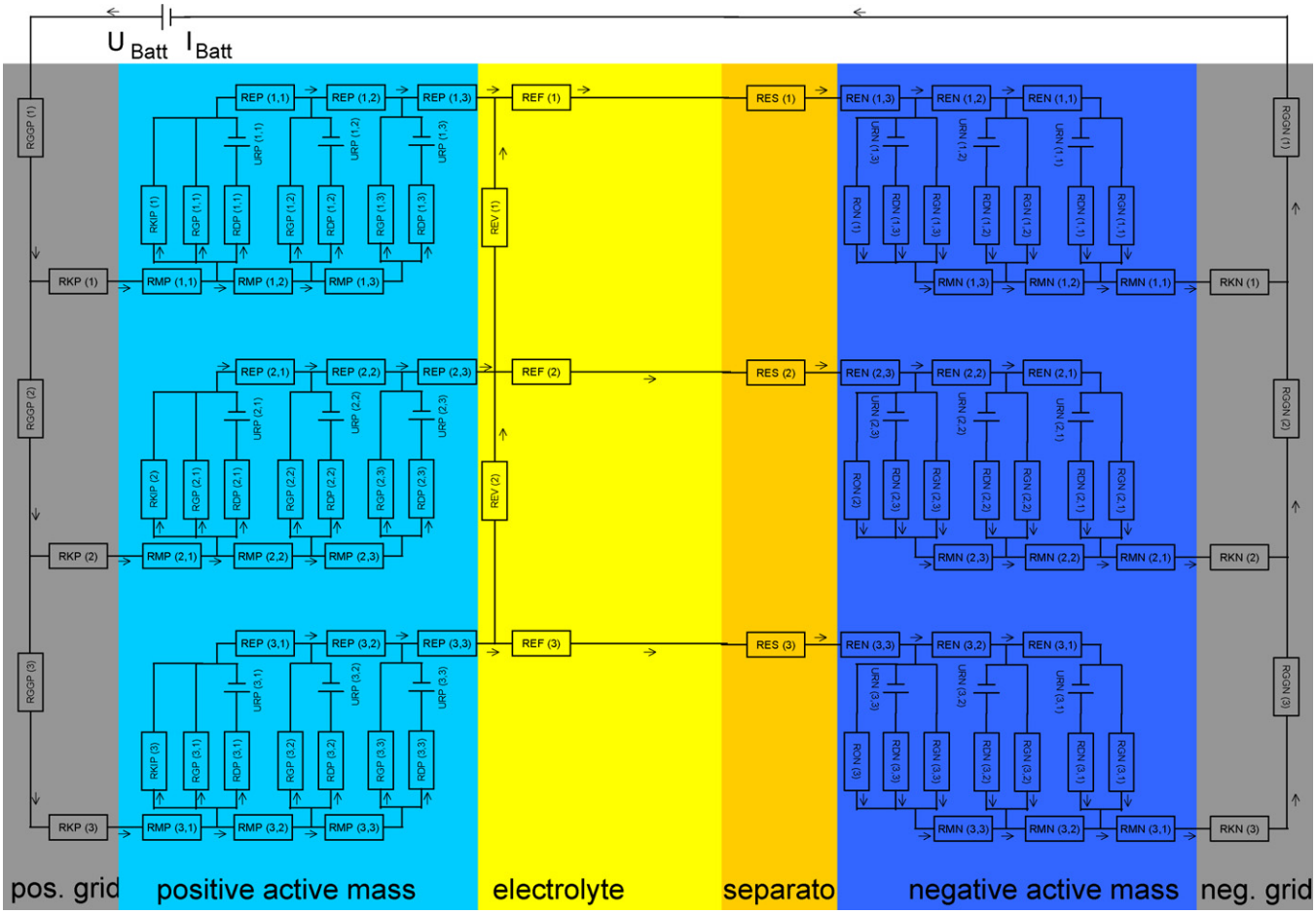

Fig. 2. Resistance network of the simulation model divided into positive and negative grid, positive and negative active mass, electrolyte and separator.

tration, state of charge and temperature. The Kirchhoff equations resulting from the equivalent electric circuit diagram are used for solving the differential equations.

2.2. Assumed process for the main reaction

The relationship between overvoltage and current flow within the main reaction is described by the well known Butler–Volmer equation. However, other than in other models it is used here in its original full version, which takes into account separate ion concentrations as the limiting factor for the anodic and the cathodic reaction on both electrodes. This also links the Pb^{2+} ion concentration with the current/voltage relation. The assumption behind this approach is that the reaction mechanism is a dissolution and crystallisation process, which means that the Pb^{2+} ion concentration is not constant, but depends on several parameters such as potential and state of charge. Eqs. (2.1) and (2.2) give the full description of the Butler–Volmer equation for the positive electrode and for the

Table 1
Meaning of the different resistances in the equivalent circuit diagram (Fig. 2).

RGGP/RGGN	Resistance of the positive/negative grid along the height of the electrode (depending on the remaining grid thickness taking into account grid corrosion)
RKP/RKN	Resistance of the corrosion layer of the positive/negative electrode (depending on the corrosion process), for the negative electrode, the resistance is zero, it is only added for symmetry
RMP/RMN	Resistance of active material of the positive/negative active mass (depending on porosity, state of charge and temperature)
RRK	Pathway for corrosion current, resistance calculated accordingly
RGP/RGN	Pathway for gassing current at the positive/negative electrode, resistance calculated according to gassing reaction (depending on electrode potential, temperature, active surface and acid concentration)
RDP/RDN	Pathway for main reaction current at positive/negative electrode, leading to a charge or discharge of the electrode, resistance calculated from the Butler–Volmer equation (depending on potential, temperature, active surface, and acid and Pb^{2+} concentration)
URP/URN	Electrochemical voltage source of positive/negative electrode, depending on acid concentration and temperature
REP/REN	Resistance of the electrolyte within the porous positive/negative electrode (depending on porosity, acid concentration and temperature)
REF	Resistance of the electrolyte in the free electrolyte volume between the positive and the negative electrode (depending on acid concentration and temperature)
RES	Resistance of the electrolyte in the separator between the positive and the negative electrode (depending on acid concentration, porosity of the separator and temperature)
REV	Vertical resistance of the electrolyte in the free electrolyte volume between the electrodes (depending on acid concentration and temperature)
RO_2	Pathway for the gas recombination current (only used in VRLA batteries) in the negative electrode, resistance calculated from the amount of gas that diffuses from the positive to the negative electrode

negative electrode respectively [17]:

$$i^+_{MR} = i^+_0 A^+_{active}\left[\left(\frac{c^+_{Pb^{2+}}}{c^0_{Pb^{2+}}}\right)^{\gamma_{Pb^{2+}}}\exp\left(\frac{\alpha^+\cdot n\cdot F}{R\cdot T}\cdot\eta^+_{act}\right)-\left(\frac{c^+_{H_2SO_4}}{c^0_{H_2SO_4}}\right)^{\gamma_{H_2SO_4}}\exp\left(-\frac{(1-\alpha^+)\cdot n\cdot F}{R\cdot T}\cdot\eta^+_{act}\right)\right] \quad (2.1)$$

$$i^-_{MR} = i^-_0 A^-_{active}\left[\left(\frac{c^-_{H_2SO_4}}{c^0_{H_2SO_4}}\right)^{\gamma_{H_2SO_4}}\exp\left(\frac{\alpha^-\cdot n\cdot F}{R\cdot T}\cdot\eta^-_{act}\right)-\left(\frac{c^-_{Pb^{2+}}}{c^0_{Pb^{2+}}}\right)^{\gamma_{Pb^{2+}}}\exp\left(-\frac{(1-\alpha^-)\cdot n\cdot F}{R\cdot T}\cdot\eta^-_{act}\right)\right] \quad (2.2)$$

where A_{active} is the active mass surface that takes part in the reaction, i.e. that is not covered by lead sulphate, as a function of local porosity [11]:

$$A_{active} = \frac{3(1-\varepsilon_{max})V\cdot\chi^{2/3}}{r_0} - \pi\cdot r^2_{PbSO_4}(SOC)N_{PbSO_4}(SOC)V \quad (2.3)$$

A_{max} is the maximum active mass surface (of a fully charged battery), ε_{max} is the porosity of a fully charged battery, V is the volume of the element, r_{PbSO_4} is the average radius, N_{PbSO_4} is the number of sulphate crystals per volume and r_0 is the radius of PbO_2 or Pb crystals of a fully charged battery.

2.3. Acid distribution–diffusion, acid stratification, gassing

In contrast to other battery technologies, the electrolyte of lead-acid batteries, sulphuric acid takes part in the main reaction. It is consumed during discharging and produced and released from the active masses during charging. Hence, acid concentration changes during charging and discharging. The average acid concentration in the battery cell is directly related to the state of charge of the battery. However, there are significant gradients within the cell caused by consumption and release of sulphuric acid in the bulk active material. Concentration gradients can be observed in horizontal direction throughout the pores of the active material and in vertical direction, known as acid stratification.

The simulation model only considers cells in upright position. Typical differences in the physics of acid distribution in VRLA and flooded batteries are taken into account.

The acid concentration in a one-dimensional approach is shown in the following equations for the electrolyte inside the positive active mass (2.4), the electrolyte inside the negative active mass (2.5) and the electrolyte in the free electrolyte or the separator between the electrodes (2.6):

$$\varepsilon\cdot\frac{\partial c_{H_2SO_4}}{\partial t} = -c_{H_2SO_4}\cdot\frac{\partial\varepsilon}{\partial t}+\frac{\partial}{\partial x}\left(\varepsilon^{ex}\cdot D\cdot\frac{\partial c_{H_2SO_4}}{\partial x}\right) + \frac{3-2t^0_+}{2F}\cdot i_{MR}+\frac{1-t^0_+}{F}\cdot i_{gas} \quad (2.4)$$

$$\varepsilon\cdot\frac{\partial c_{H_2SO_4}}{\partial t} = -c_{H_2SO_4}\cdot\frac{\partial\varepsilon}{\partial t}+\frac{\partial}{\partial x}\left(\varepsilon^{ex}\cdot D\cdot\frac{\partial c_{H_2SO_4}}{\partial x}\right) + \frac{1-2t^0_+}{2F}\cdot i_{MR}+\frac{1-t^0_+}{F}\cdot i_{gas} \quad (2.5)$$

$$\varepsilon\cdot\frac{\partial c_{H_2SO_4}}{\partial t} = \varepsilon^{ex}\cdot D\cdot\frac{\partial^2 c_{H_2SO_4}}{\partial x^2} \quad (2.6)$$

For a two-dimensional approach, some additional assumption is necessary, especially concerning gravity effects and gassing. Furthermore, for the implementation some simplifications of the mathematics are necessary.

The following sections describe how the acid distribution within the cell is modelled.

2.3.1. Basic model and electrochemical reactions

Active masses are converted from PbO_2 or Pb to $PbSO_4$ during discharging by using sulphate ions from the electrolyte (Eq. (2.7)). This results in a depletion of sulphate ions during discharging and in an enrichment of sulphate ions during charging. Concentration gradients are directly correlated with density gradients, which result in acid stratification caused by gravity forces (Eq. (2.9)) and concentration gradients result in diffusion forces (Eq. (2.12)). Gravity forces result in a vertical density gradient within the battery cell, diffusion tends to homogenise the concentration gradients. The model generally assumes a fully homogenised electrolyte concentration after infinitely long times. This implies that sulphuric acid is treated as a single phase liquid which has no tendency on its own to build up any concentration or density gradients. However levelling out all concentration gradients takes very long times, especially in vertical directions and in tall cells. Another factor influencing the local acid concentration is gassing: gas bubbles result in a mixing and thus a homogenisation of the electrolyte (Eq. (2.17)). In the case of gel or AGM batteries, the contributions of concentration changes due to both gassing and buoyancy/gravity are assumed to be zero.[4]

For the modelling the following assumptions are made:

- Sulphuric acid is dissociated by 100% in the first step ($H_2SO_4 \rightarrow H^+ + HSO_4^-$).
- The second dissociation step does not occur.
- The proton concentration caused by the dissociation of water ($H_2O \rightarrow H^+ + OH^-$) is neglected.
- Sulphuric acid is assumed as a single phase liquid with no tendency to separate into water and concentrated sulphuric acid.

The following sections describe in brief the basics of the implementation of the different parts of the model. In all parts of the model, the change in the number of moles of H_2SO_4 in each volume elements is calculated instead of concentration gradients $c = N/V$ to simplify the model equation because V is assumed to be constant within one time step.

2.3.2. Ion source and sink

Caused by the main reaction current, sulphate ions are released to the electrolyte (ion source during charging) or taken from the electrolyte (ion sink during discharging). Therefore the local acid concentration and the acid density change with the main reaction current i_{MR} and the gassing current i_{gas} according to Eq. (2.7):

$$\left.\frac{\partial N}{\partial t}\right|_{source/sink} = \frac{3-2t^0_+}{2F}i_{MR}+\frac{1-t^0_+}{F}i_{gas} \quad \text{(positive electrode)}$$
$$\left.\frac{\partial N}{\partial t}\right|_{source/sink} = \frac{2t^0_+-1}{2F}i_{MR}+\frac{t^0_+-1}{F}i_{gas} \quad \text{(negative electrode)} \quad (2.7)$$

t^+_0 is the Hittorf number (typical value: 0.7).

[4] In reality (small) concentration gradients due to gravity also occur in AGM batteries, which is strongly dependent on the quality of the glass mat. In low quality mats, the capillary forces are too small to counteract the gravity forces. However, this effect is hard to represent in a model and typically neglectable.

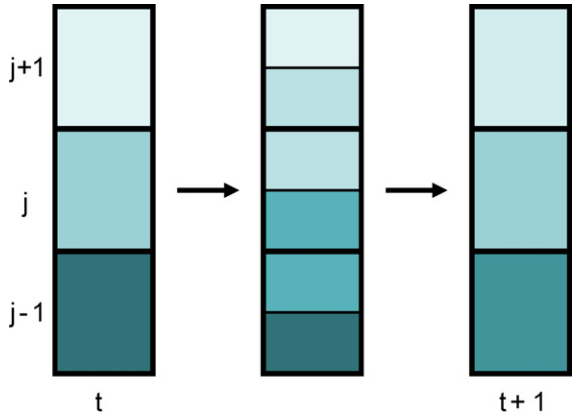

Fig. 3. Electrolyte mixing due to buoyancy.

2.3.3. Buoyancy/gravity

If a certain electrolyte volume with density ρ_j, e.g. created in a pore during charging, moves within an infinite surrounding fluid with density ρ_{j+1}, e.g. the remaining electrolyte, it is assumed that the velocity of the small volume can be calculated according to Eq. (2.8). The velocity depends on a geometry parameter b, the viscosity η of the electrolyte and the density difference:

$$v = \frac{8gb^2}{\eta}(\rho_j - \rho_{j+1}) \quad \forall \rho_j > \rho_{j+1} \tag{2.8}$$

It is assumed that the velocity remains unchanged within one time step. The number of moles N that moves from element j to element $j+1$, which is directly above element j, can be calculated according to Eq. (2.9):

$$\left.\frac{\partial N_j}{\partial t}\right|_{\text{buoyancy}} = \frac{1}{2}\left(\frac{v_{j-1}}{h_{j-1}}N_{j-1} - \frac{v_{j-1}}{h_j}N_j\right) + \frac{1}{2}\left(\frac{v_j}{h_{j+1}}N_{j+1} - \frac{v_j}{h_j}N_j\right) \tag{2.9}$$

where h is the height of the volume. Fig. 3 illustrates the electrolyte movement due to buoyancy: in the left picture, three volume elements on top of each other are shown at time t. Element $j-1$ has the largest number of moles and element $j+1$ has the smallest number. Due to buoyancy, some moles move from element $j-1$ to element j, which results in a new average concentration in the upper half of element $j-1$ and the lower half of element j. The exchange between j and $j+1$ works similarly. Then, a new concentration for each element is calculated, which is then used in time step $t+1$.

2.3.4. Diffusion

Diffusion is based on Fick's second law:

$$\frac{\partial c}{\partial t} = D\nabla^2 c \tag{2.10}$$

where $c = N/V$ is the electrolyte concentration, which is the number of moles of H_2SO_4 per volume element V and D is the diffusion coefficient of H_2SO_4. To decouple the equation, in the implementation the volume V of a volume element is assumed to be constant within one time step, so that Eq. (2.10) can be written as:

$$\frac{1}{V}\frac{\partial N}{\partial t} = D\nabla^2\left(\frac{N}{V}\right) \tag{2.11}$$

The volume can change due to water loss (above the electrodes) or changes in the porosity of the active masses (inside the electrodes). As this is a very slow process compared to the change of the number of moles, the error to consider V as constant during one time step is very small.

For the two-dimensional case, Eq. (2.11) becomes Eq. (2.12):

$$\frac{1}{V}\frac{\partial N}{\partial t} = D\left(\frac{\partial^2(N/V)}{\partial x^2} + \frac{\partial^2(N/V)}{\partial y^2}\right) \tag{2.12}$$

2.3.5. Gassing

Gassing causes a mixing of the electrolyte. It is assumed that each gas bubble with a certain volume causes mixing of the electrolyte in volume elements above the current element. Only the overall gas volume is of relevance in this model. Hydrogen evolution is assumed to occur close to the negative electrode and oxygen evolution close to the positive electrode.

The gassing current at positive (2.13) and negative electrode (2.14) is calculated according to the Butler–Volmer equation:

$$i^+_{\text{gas}} = i^+_{0,\text{gas}} \cdot A^+_{\max}\left(\frac{\varepsilon(\text{SOC}) - \varepsilon_{\min}}{\varepsilon_{\max} - \varepsilon_{\min}}\right)^{\zeta_1} \exp\left(\frac{\alpha_{\text{gas}} \cdot n \cdot F}{R \cdot T} \cdot \eta^+_{\text{gas}}\right) \tag{2.13}$$

$$i^-_{\text{gas}} = i^-_{0,\text{gas}} \cdot A^-_{\max}\left(\frac{\varepsilon(\text{SOC}) - \varepsilon_{\min}}{\varepsilon_{\max} - \varepsilon_{\min}}\right)^{\zeta_1} \exp\left(-\frac{(1-\alpha_{\text{gas}}) \cdot n \cdot F}{R \cdot T} \cdot \eta^-_{\text{gas}}\right) \tag{2.14}$$

Gassing is a very complex process with strong dependencies on local conditions, such as the size of the gas bubbles, their free path through the electrolyte, pore size and more. Since these local conditions cannot be represented and parameterised sufficiently, a semi-empirical approach is chosen with one single fit parameter f (Eq. (2.17)) that can be obtained from measurements.

For the acid movement, first of all the volume of the gas is calculated (Eq. (2.15)), which depends on the gassing current i^{gas}. The gas volume accumulates with increasing height y in the cell:

$$\frac{\partial V^{\text{gas}}(y)}{dt} = \frac{R \cdot T}{n \cdot F \cdot p(y)} \int_{h_{\text{below}}}^{y} i^{\text{gas}}(y')\, dy' \tag{2.15}$$

$R = 8.314\,\text{J K}^{-1}\,\text{mol}^{-1}$ is the gas constant, $n = 2$ is the number of electrons, $F = 96{,}485\,\text{C mol}^{-1}$ is Faraday's constant and T is the absolute temperature in the volume element. Furthermore, the volume depends on the pressure (Eq. (2.16)) in the volume element:

$$p(y) = p_{\text{ambient}} + \int_{y}^{\text{upper electrolyte level}} \rho(y')g\, dy' \tag{2.16}$$

The resulting change in the number of moles due to gassing is calculated according to Eq. (2.17):

$$\left.\frac{\partial N}{\partial t}\right|_{\text{gassing}} = f\frac{N}{V}\frac{\partial V^{\text{gas}}}{\partial t} \tag{2.17}$$

where f is an experimental factor that describes the efficiency of electrolyte mixing by gas bubbles.

Please note that gassing has no mixing effect in the electrolyte volume below the electrodes. Furthermore the mixing process is most efficient in the upper part as all gas generated along the electrode height is accumulated here.

2.3.6. Calculation of the acid distribution

The overall acid distribution is calculated from the superposition of the effects described above (Eq. (2.18)):

$$\frac{\partial N}{\partial t} = \left.\frac{\partial N}{\partial t}\right|_{\text{diffusion}} + \left.\frac{\partial N}{\partial t}\right|_{\text{buoyancy}} + \left.\frac{\partial N}{\partial t}\right|_{\text{gassing}} + \left.\frac{\partial N}{\partial t}\right|_{\text{source/sink}} \tag{2.18}$$

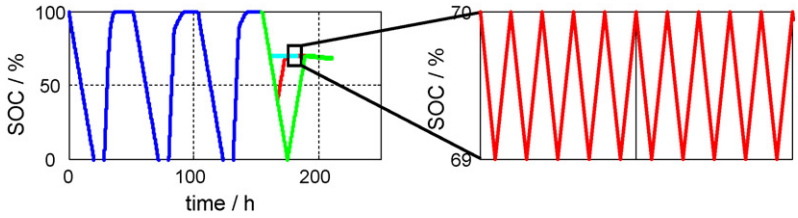

Fig. 4. SOC during simulation: blue curve, three full cycles for generation of acid stratification (optional); cyan, red; green curve, SOC preconditioning. Green: 100% → 70%, red: 100% → 40% → 70%, cyan: 100% → 0% → 70%. (For interpretation of the references to color in this figure legend, the reader is referred to the web version of the article.)

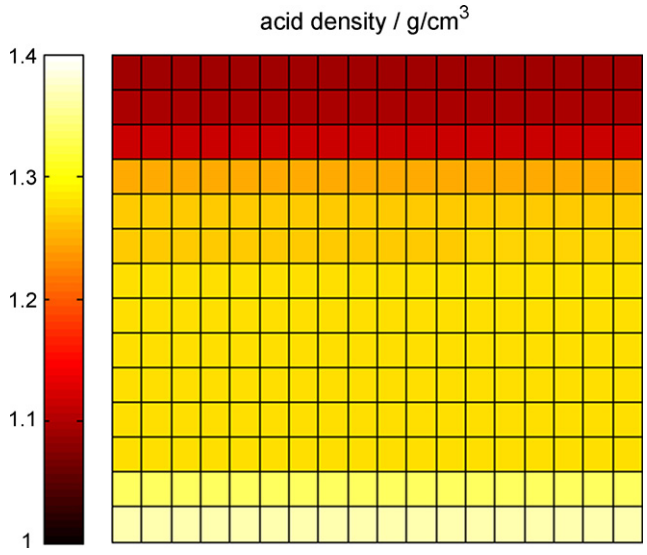

Fig. 5. Legend for acid density.

2.3.7. *Change of electrolyte volume*

The volume of the electrolyte needs to be calculated at any time to assure a correct calculation of the acid concentration. While the number of moles of sulphuric acid can be easily calculated from the Ah balance, the overall volume of the electrolyte changes according to six processes:

1. Loss of water due to gassing (in VRLA batteries only when the valve opens).
2. Change of specific volume with acid concentration.
3. Change of volume in the cell due to loss of pore volume during discharging (conversion of Pb and PbO_2 to $PbSO_4$).
4. Change of electrolyte volume with temperature.
5. Refilling of deionised water.
6. Varying gas volume in the pores.

The effective electrolyte volume of the elements in the electrodes depends on the local porosity and therefore on the local state of charge.

Table 2
variations for the micro-cycle simulations.

SOC preconditioning	Current rate for preconditioning	Acid stratification
100% → 70%	I_{20}	Without
100% → 40% → 70%	$4I_{20}$	With (after three full cycles)
100% → 0% → 70%	$20I_{20}$	

3. Simulation results

The model described above was used to investigate the impact of several parameters on acid density, charge and current distribution during micro-cycles in flooded SLI batteries.

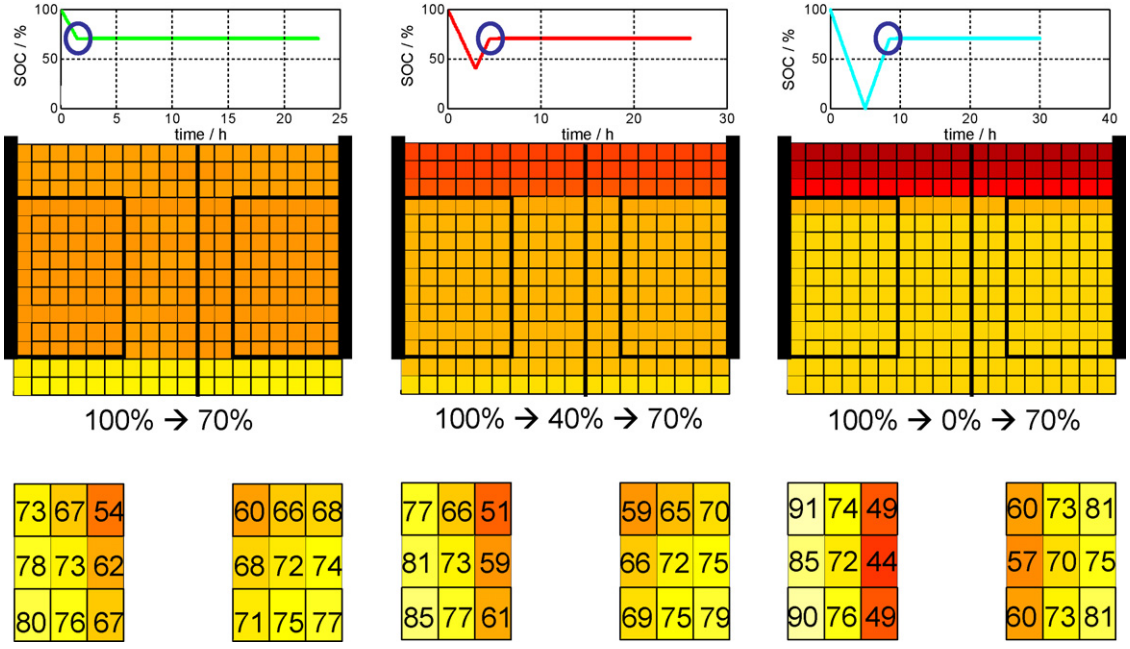

Fig. 6. Impact of SOC preconditioning; acid density (upper row) and SOC distribution in % (lower row) immediately after the preconditioning; simulation without initial acid stratification and $4I_{20}$ for preconditioning.

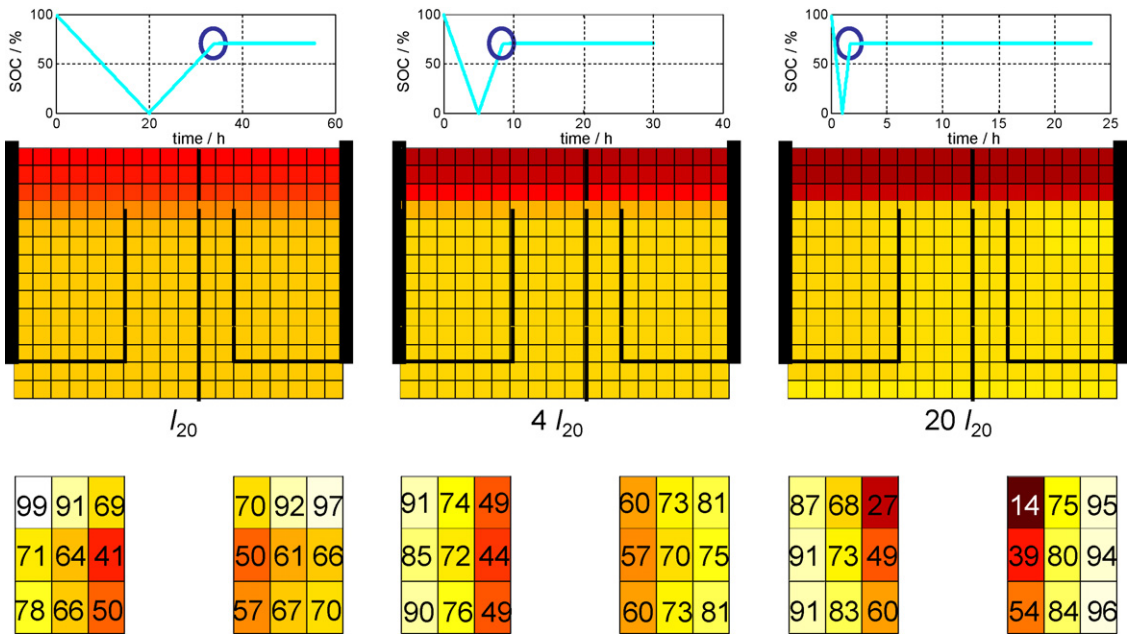

Fig. 7. Impact of current rate during preconditioning; acid density (upper row) and SOC distribution in % (lower row) immediately after the preconditioning; simulation without initial acid stratification and SOC preconditioning 100% → 0% → 70%.

3.1. Simulation profile

In order to identify the influence of short-term history parameters on acid and SOC distribution, such as charge/discharge history, current rate and initial acid stratification, different profiles (Fig. 4) were used consisting of a SOC preconditioning followed by a pause of 1 h and 1000 micro-cycles with $\pm 20 I_{20}$, each charge and discharge step has a duration of 36 s. The different parameters are given in Table 2. All combinations were simulated, which gives a total of 18 simulations.

3.2. Acid density and SOC distribution

In the following, the impact of SOC preconditioning, current rate during preconditioning, initial acid stratification and micro-cycles is illustrated based on exemplary simulations. Fig. 5 illustrates the color coding for acid density that is used in all figures.

3.2.1. SOC preconditioning

Fig. 6 shows exemplarily acid density (upper row) and charge distribution (lower row) immediately after SOC preconditioning for

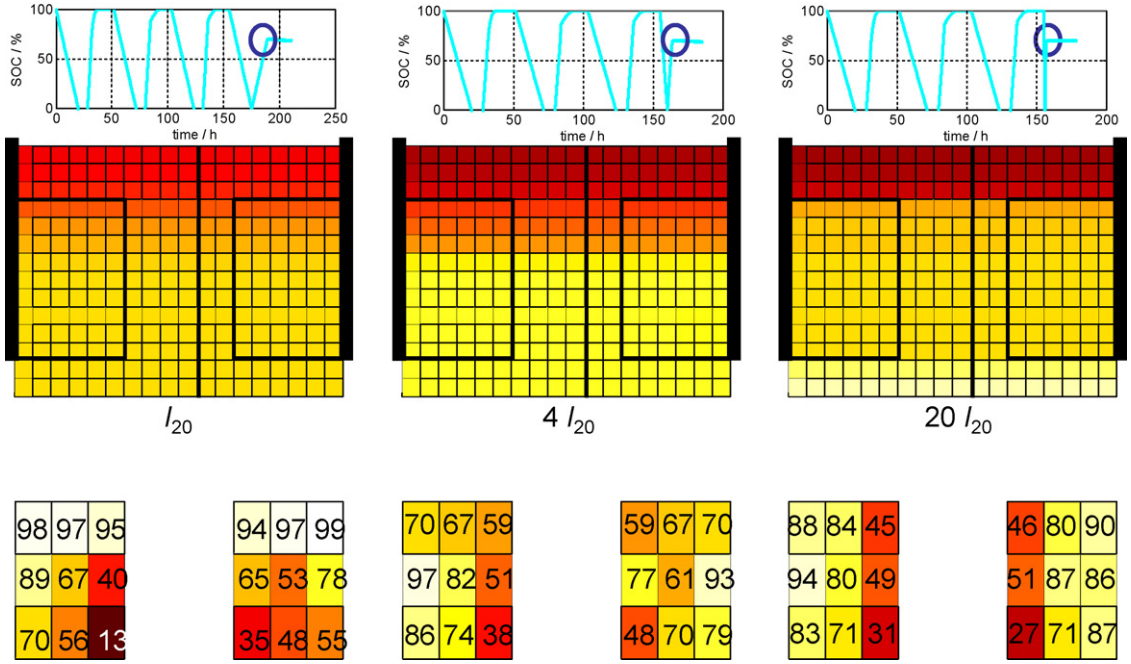

Fig. 8. Impact of initial acid stratification; acid density (upper row) and SOC distribution in % (lower row) immediately after the preconditioning; simulation with initial acid stratification and SOC preconditioning 100% → 0% → 70%.

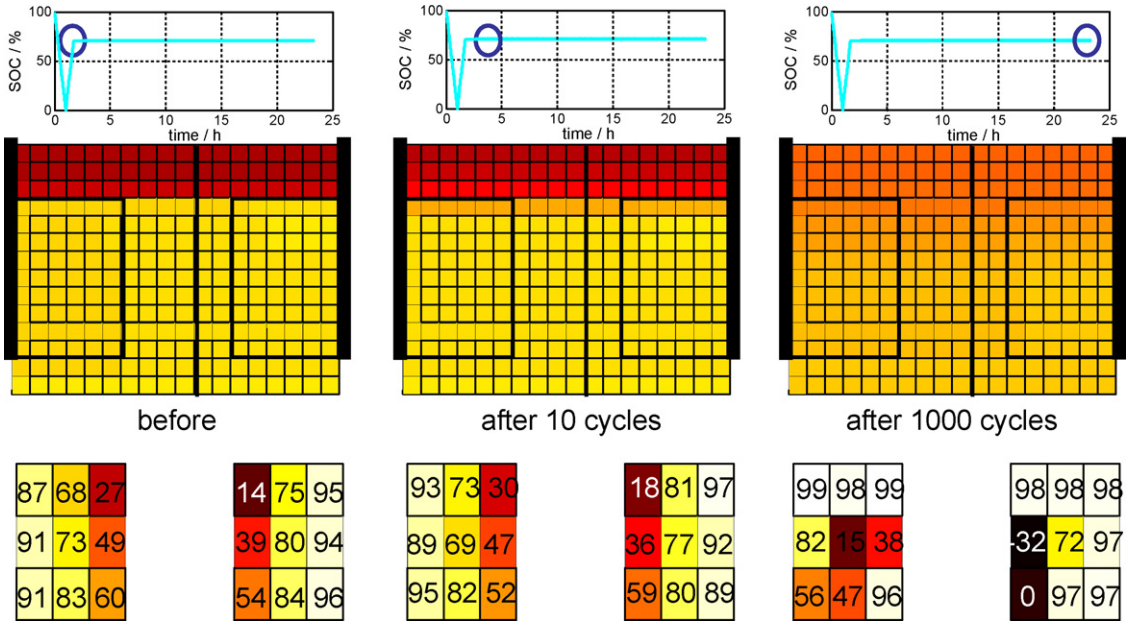

Fig. 9. Impact of micro-cycling; acid density (upper row) and SOC distribution in % (lower row) immediately after the preconditioning (left), after 10 cycles (middle) and after 1000 cycles (right); simulation without initial acid stratification and SOC preconditioning 100% → 0% → 70% with $20I_{20}$. (The low SOC in the middle part of the negative electrode after 1000 micro cycles is not in good agreement with post-mortem analyses, which show a strong sulphation of the lower part of the negative electrode. Nevertheless, it can be seen that micro cycles lead to strong inhomogeneities in the charge distribution.)

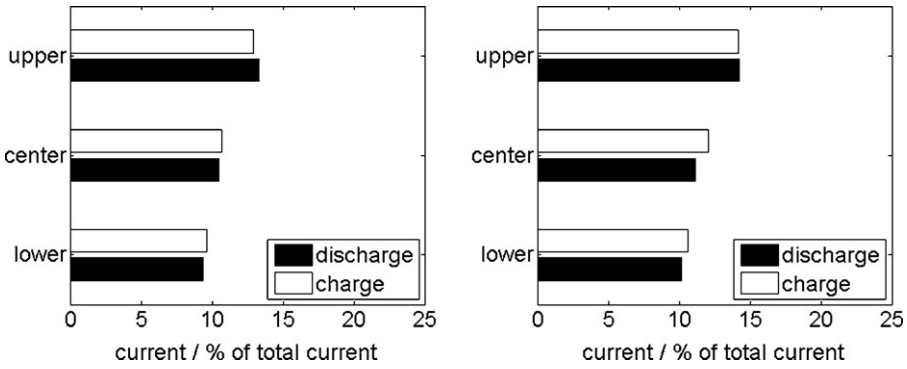

Fig. 10. Current distribution during 50th micro-cycle (left) and 900th micro-cycle (right) after SOC preconditioning 100% → 70% with I_{20} without initial acid stratification (best case).

the three cases: discharge from 100% to 70% (left), discharge from 100% to 40% and charge to 70% (middle) and discharge from 100% to 0% and charge to 70% (right). Both charge and discharge were done with a current rate of $4I_{20}$; the simulation was started without initial acid stratification. It can be seen that both acid density and charge distribution are more inhomogeneous after charging (middle and right) than after discharging (left). Gradients rise with depth of discharge and change from vertical to horizontal direction in the case of charge distribution. Similar findings result from the other simulations.

3.2.2. Current during preconditioning

Fig. 7 shows exemplarily acid density (upper row) and charge distribution (lower row) immediately after SOC preconditioning discharge from 100% to 0% and charge to 70% for the three different current rates. The simulation was started without initial acid stratification. It can be seen that inhomogeneity of both acid density and charge distribution grows with current rate. The charge distribution gradient changes from vertical to horizontal direction with increasing current rate. Similar findings result from the other simulations.

3.2.3. Initial acid stratification

Fig. 8 shows exemplarily acid density (upper row) and charge distribution (lower row) immediately after SOC preconditioning discharge from 100% to 0% and charge to 70% for the three different current rates. In contrast to Fig. 7, the simulation was started with initial acid stratification under the same conditions in all other respects. In comparison with Fig. 7, the same qualitative impact of current rate can be observed, but with significantly larger gradients.

3.2.4. Micro-cycles

Fig. 9 shows exemplarily acid density (upper row) and charge distribution (lower row) immediately after SOC preconditioning, in the 10th micro-cycle and in the 1000th micro-cycle after discharge from 100% to 0% and charge to 70% with $20I_{20}$. During the micro-cycles, acid stratification is gradually removed and after 1000 cycles, acid density is nearly homogeneous in the battery. By contrast, charge distribution becomes more and more inhomogeneous. This is because the upper part of the electrodes is charged much more than the lower part due to an inhomogeneous current distribution caused by initial inhomogeneities (see Section 3.3).

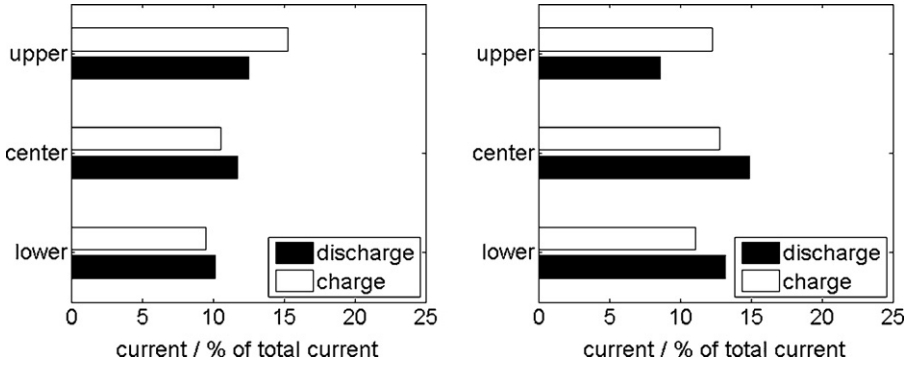

Fig. 11. Current distribution during 50th micro-cycle (left) and 900th micro-cycle (right) after SOC preconditioning 100% → 0% → 70% with 20 I_{20} with initial acid stratification (worst case).

3.3. Current distribution

In the following, only the micro-cycles are considered. Figs. 10 and 11 show the current distribution in the positive electrode[5] in the 50th and 900th micro-cycle during charging and discharging for two different sets of conditions: SOC preconditioning 100% → 70% with I_{20} without initial acid stratification (Fig. 10) and SOC preconditioning 100% → 0% → 70% with $20I_{20}$ with acid stratification (Fig. 11). The first set of conditions represents the best case of all simulations concerning inhomogeneities and the second set represents the worst case. It can be seen that current distribution and especially location of charge and discharge depends strongly on the conditions of the battery. Acid stratification, charging and large currents (Fig. 11) lead to large differences in the location of charging and discharging: while the discharging current in the 50th cycle is more or less equal in the upper, middle and lower part of the electrodes, nearly half of the charging current goes to the upper part of the electrodes. In the 900th cycle, the differences become even worse and about one-third of the current goes to the lower part during discharging, while only about one-fourth is charged back to the lower part during the next charging step. In contrast to this, no initial acid stratification, discharging and small currents (Fig. 10) lead to a more homogeneous location of charging and discharging currents. The impact of inhomogeneous current distribution between charging and discharging can clearly be seen by the differences in the charge distribution (see Fig. 9): the upper part of the electrodes is almost fully charged after the micro-cycles, while the lower part is more discharged. However, in the 900th cycle, still about 40% of the charging current goes to the upper part of the electrode, although it cannot accept much more charge.

4. Conclusion

Simulations have shown the impact of short-term history parameters such as current rate, acid distribution, charge or discharge history and micro-cycling on acid density and charge distribution in flooded SLI batteries. It was found that large current rates, large depth of discharge, charge history and initial acid stratification increase inhomogeneities in both acid density and charge distribution. Micro-cycles homogenise acid density distribution, but raise gradients in charge distribution. Initial inhomogeneities before micro-cycling lead to an inhomogeneous current distribution and local variation of charge balance, which increase the inhomogeneous charge distribution. Even a slight deviation from symmetry of local charge balances may, over thousands of micro-cycles, lead to a material distribution in the electrodes that limits the dynamic charge acceptance dramatically.

[5] The current distribution in the negative electrode is nearly the same.

References

[1] A. Jossen, J. Garche, D.U. Sauer, Sol. Energy 76 (2004) 759–769.
[2] P. Ruetschi, J. Power Sources 127 (2004) 33–44.
[3] D.U. Sauer, et al., An analysis of strongly varying dynamic charge acceptance in SLI batteries in micro hybrid applications, in: Presentation at 11th ELBC, Warsaw, 2008.
[4] D.U. Sauer, et al., J. Power Sources 168 (2007) 22–30.
[5] P.T. Moseley, R.F. Nelson, A.F. Hollenkamp, J. Power Sources 157 (2006) 3–10.
[6] J. Valenciano, A. Sanchez, F. Trinidad, A.F. Hollenkamp, J. Power Sources 158 (2006) 851–863.
[7] M. Calábek, K. Micka, P. Křivák, P. Bača, J. Power Sources 158 (2006) 864–867.
[8] K. Sawai, et al., J. Power Sources 158 (2006) 1084–1090.
[9] J. Newman, W. Tiedemann, AIChE J. 21 (1975) 25–41.
[10] W.G. Sunu, in: R.E. White (Ed.), Electrochemical Cell Design, Plenum Press, New York, London, 1984, pp. 357–376.
[11] H. Gu, T.V. Nguyen, R.E. White, J. Electrochem. Soc. 134 (1987) 2953–2960.
[12] D.M. Bernardi, H. Gu, A.Y. Schoene, J. Electrochem. Soc. 140 (1993) 2250–2258.
[13] F. Alavyoon, A. Eklund, F.H. Bark, R.I. Karlsson, D. Simonsson, Electrochim. Acta 36 (1991) 2153–2164.
[14] W.B. Gu, C.Y. Wang, B.Y. Liaw, J. Electrochem. Soc. 144 (1997) 2053–2061.
[15] D.U. Sauer, J. Power Sources 64 (1997) 181–187.
[16] D.U. Sauer, J. Garche, J. Power Sources 95 (2001) 130–134.
[17] D.U. Sauer, Optimierung des Einsatzes von Blei-Säure-Akkumulatoren in PV-Hybrid-Systemen unter spezieller Berücksichtigung der Batteriealterung, PhD Thesis, University of Ulm, Germany, 2003.
[18] R.J. Ball, R. Evans, R. Stevens, J. Power Sources 103 (2002) 213–222.
[19] P. Král, P. Křivák, M. Calábek, K. Micka, J. Power Sources 105 (2002) 35–44.
[20] P. Křivák, P. Bača, M. Calábek, K. Micka, P. Král, J. Power Sources 154 (2006) 518–522.
[21] V. Boovaragavan, V.R. Subramanian, J. Power Sources 173 (2007) 1006–1011.
[22] M. Calábek, K. Micka, P. Bača, P. Křivák, J. Power Sources 85 (2000) 145–148.
[23] V. Svoboda, H. Doering, J. Garche, J. Power Sources 144 (2005) 244–254.
[24] M. Thele, J. Schiffer, E. Karden, E. Surewaard, D.U. Sauer, J. Power Sources 168 (2007) 31–39.